Simulation Study of Using High-Z EMA to Suppress Recoil Protons Crosstalk in Scintillating Fiber Array for 14.1 MeV Neutron Imaging

Qinggang Jia, Huasi Hu, Fengna Zhang, Tiankui Zhang, Wei Lv, Yuanpin Zhan, and Zhihua Liu

***Abstract*—This paper studies the effect of a high-Z extra mural absorber (EMA) to improve the spatial resolution of a plastic (polystyrene) scintillating fiber array for 14.1 MeV fusion neutron imaging. Crosstalk induced by recoil protons was studied, and platinum (Pt) was selected as EMA material, because of its excellent ability to suppress the recoil protons penetrating the fibers. Three common fiber arrays (cylindrical scintillating fibers in square and hexagonal packing arrangements and square scintillating fibers) were simulated using the Monte Carlo method for evaluating the effect of Pt-EMA in improving spatial resolution. It is found that the resolution of the 100 μm square fiber array can be improved from 1.7 to 3.4 lp/mm by using 10-μm-thick Pt-EMA; comparatively, using an array with thinner square fibers (50 μm) only obtains a resolution of 2.1 lp/mm. The packing fraction decreases with the increase of EMA thickness. Our results recommend the use of 10 μm Pt-EMA for the square and the cylindrical (hexagonal packing) scintillating fiber arrays with fibers of 50–200 μm in the cross-sectional dimension. Besides, the dead-zone material should be replaced by high-Z material for the hexagonal packing cylindrical fiber array with fibers of 50–200 μm in diameter. Tungsten (W) and gold (Au) are also used as EMA in the three fiber arrays as a comparison. The simulation results show that W can be used at a lower cost, and Au does not have any advantages in cost and resolution improvement.**

***Index Terms*—Extra mural absorber (EMA), fusion neutron imaging, Geant4, recoil proton crosstalk, resolution, scintillating fiber array.**

I. Introduction

IN INERTIAL confinement fusion (ICF) experiments, the diagnosis of the spatial distribution of 14.1 MeV neutrons emitted from the reaction area provides useful information about the symmetry of implosion. The images of fusion neutrons are often obtained by using a scintillating fiber array detector due to its inherent spatial resolution [1]–[11]. Thin fibers, such as those with a diameter of 65 μm [1], are adopted for better resolution. However, the fiber size is already much smaller than the average diameter of the light response range of 14.1 MeV incident neutrons in scintillation material, which is calculated to be 500 μm [2]. Substituting the fibers with thinner ones may not effectively improve spatial resolution. In the scintillator, an incident neutron mainly transfers its energy to the light nuclei hydrogen through scattering. In the array with thin fibers, the scattered neutrons and recoil protons can easily penetrate into other fibers. This effect is called crosstalk, which leads to deterioration of the image contrast and spatial resolution.

Over the years, a number of methods have been employed to alleviate the crosstalk effect. One of them is to improve the scintillation material, such as increasing the ratio of carbon to hydrogen [3] and replacing hydrogen with deuterium [4]. Nevertheless, these materials are inherently of low sensitivity due to the quenching effect. Another method, based on deconvolution algorithms, is developed for restoring the contrast and the spatial resolution of fast fusion neutron images [12], [13]. Yet, this unfolding method will give rise to an extra distortion on the image when the neutron intensity is low.

High-Z materials, called extra mural absorber (EMA) are normally employed to reduce the cross-talk induced by photons or gamma rays [14]–[16]. In fusion neutron imaging, high-Z paint and aluminum cladding were used as EMA for preventing the recoil proton cross-talk in the scintillating fiber arrays [5], [11]. However, to the best of our knowledge, there is no report on the evaluation of EMA performance. Theoretically, the intrinsic spatial resolution should be improved with the EMA thickness if only cross-talk effect is under consideration. However, the use of EMA enlarges the pixel (fiber and EMA) size and may result in a reduction of spatial resolution. Since EMA leads to an extra dead zone in the fiber array detector, the packing fraction [12], which represents the sensitive area fraction of the array, should also be taken into account. The cross-section of fibers and the packing formation type also affect the performance of EMA in scintillating fiber array detectors.

This study investigates the performance of high-Z EMA in improving the spatial resolution of scintillating fiber arrays for 14.1 MeV neutron imaging. The Monte Carlo simulation toolkit Geant4 [17], [18] is used to simulate the crosstalk effect, and MCNPX [19] is adopted for the code-to-code verification. Platinum (Pt) is selected as EMA material because of its excellent ability to suppress the recoil protons penetrating the fibers. As a comparison, tungsten (W) and gold (Au) are also used. Three

Manuscript received June 14, 2012; revised July 31, 2012; accepted October 17, 2013. Date of publication December 03, 2013; date of current version December 11, 2013. This work was supported in part by the National Natural Science Foundation of China (10975113) and in part by the Innovative Research Team in University of Ministry of Education of China (Nuclear Energy Science and Engineering under Grant IRT1280).

Q. Jia, H. Hu, F. Zhang, T. Zhang, Y. Zhan, and Z. Liu are with the School of Nuclear Science and Technology, Xi'an Jiaotong University (XJTU), Xi'an, 710049 Shannxi, China (e-mail: huasi_hu@mail.xjtu.edu.cn; jackgone@stu.xjtu.edu.cn; 575821277@qq.com; china-ztk@stu.xjtu.edu.cn).

W. Lv is with the University of Illinois at Urbana-Champaign, Urbana, IL 61801 USA (e-mail: weilv2@illinois.edu).

Color versions of one or more of the figures in this paper are available online at http://ieeexplore.ieee.org.

Digital Object Identifier 10.1109/TNS.2013.2289987

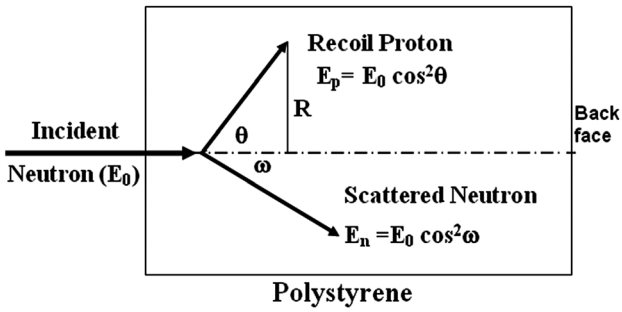

Fig. 1. Brief demonstration of recoil protons generated by neutron scattering.

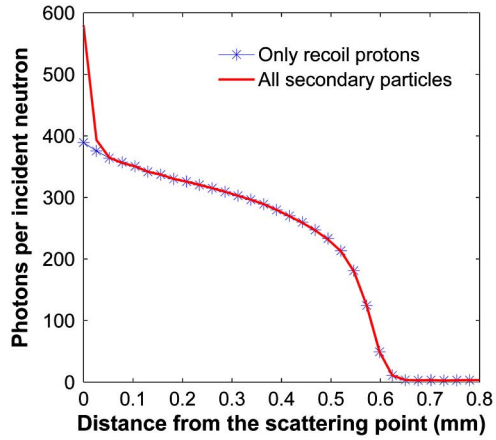

Fig. 2. Light response of a 14.1 MeV neutron impinging on polystyrene versus the distance (perpendicular to the incident neutron direction) from the interaction point for two cases with relative standard deviation <5% (RSD). The red one shows the result of considering all secondary particles while the blue one gives the result if only the recoil proton is involved.

common fiber arrays, namely, cylindrical scintillating fibers in square and hexagonal packing arrangements and square scintillating fibers, were simulated for the evaluation of Pt, W, and Au EMA performances. The applicability of the three kinds of EMA on the spatial resolution and packing fraction under various conditions is presented.

II. Crosstalk in Plastic Fibers

In plastic scintillating fiber, a fusion neutron may transfer its energy through several competing interactions, including that with hydrogen nucleus, such as $\mathrm{H}(n,n)\mathrm{H}$ and $\mathrm{H}(n,\gamma)\mathrm{D}$, and that with carbon nucleus, such as $^{12}\mathrm{C}(n,n)^{12}\mathrm{C}$, $^{12}\mathrm{C}(n,n\gamma)^{12}\mathrm{C}$, $^{12}\mathrm{C}(n,\alpha)^{9}\mathrm{Be}$, and $^{12}\mathrm{C}(n,n')3\alpha$ [20]. The secondary charged particles induced by the neutron will produce light along their tracks. Although the cross-section for the interaction between the 14.1 MeV neutron and the $^{12}\mathrm{C}$ nucleus (1.5 barns) [21] is larger than that for the interaction between neutron and hydrogen nucleus (0.7 barns), the neutron can transfer less kinetic energy to $^{12}\mathrm{C}$ than to hydrogen. Furthermore, due to the quenching effect, the heavily charged particles will produce less light than the recoil protons with the same energy [20]. Elastic scattering of 14.1 MeV neutrons is the principal light production mechanism in scintillation material. Fig. 1 gives a brief illustration of light response induced by recoil protons. When an incident neutron ends up with an interaction in polystyrene, a recoil proton is generated. The proton can travel a distance R from the line of flight of the incident neutron. The energy and direction of the recoil proton can be determined using a simple equation as follows:

$$E_p = E_0 \cos^2\theta \tag{1}$$

where E_p is the recoil proton energy, E_0 is the incident neutron energy, and θ is the recoil proton scattering angle.

The light yield distribution produced by the 14.1 MeV neutron impinged on a 1-cm-thick polystyrene (C_8H_8, 1.05 g/cm^3) slab is simulated using Geant4 (version 9.3). The high precision (HP) neutron physics models (G4NeutronHPElastic, G4NeutronHPInelastic, G4NeutronHPCapture, and G4NeutronHPFission) are chosen which simulate the interaction of neutrons with energies from thermal to 20 MeV. The neutron cross-section data are provided by Geant4's G4NDL3.13 library, in which data are largely derived from the ENDF/B-VI evaluated data library [21]. The standard electromagnetic process, called EM package (G4EMLOW.6.9) [22], is used as well. Based on the various interaction models, the information about the neutron and all of the secondary particles is recorded in each step along their trajectories. In the scintillation process, the relationship between proton energy deposition and the light yield is nonlinear due to the quenching effect. It follows Birks law and can be obtained from experimental data [23]. In Geant4, the model for the Birks law is described by a semi-empirical formula

$$\mathrm{L}_{\mathrm{E}_0} = \int_0^{\mathrm{E}_0} \frac{S\mathrm{dE}}{1 + kB(dE/dx)} \tag{2}$$

where E_0 is the initial particle energy, dE/dx is the specific energy loss, and the constant parameter S is 8000 photons per 1 MeV electron energy (MeVee) absorbed. kB of polystyrene is 0.07943 mm/MeV [24]. The range cut is set to be 1 μm. More details about this cut will be given in Section III. Ten million neutrons are used in the simulation.

Three-dimensional (3-D) light yields are recorded without tracking the scintillation photons. Then, it is integrated along the direction of incident neutron. The obtained 2-D distribution has rotational symmetry about the scattering point. The dependence of light yield on R, the distance from the scattering point, is calculated and shown in Fig. 2. The red curve gives the total light response of the neutron, while the blue one marked with an asterisk shows the contribution of recoil protons to light response. The two distributions agree with each other well, except that the red one is higher than the blue in a small range (<0.05 mm) close to the scattering point. This slight difference is mainly due to the production of heavy charged particles, such as α, $^{12}\mathrm{C}$, or $^{9}\mathrm{Be}$ near the interaction point. The result also shows that more than 90% of the light output of the incident neutron was generated by the recoil protons, which is in agreement with a previous report [25]. One thing to note is that the actual light intensity of a tiny pixel at distance r from the scattering point is equal to the light yield (red curve in Fig. 2) at r divided by $2\pi \cdot r$.

In Fig. 2, the range distribution of recoil proton varies between 0.0 and 0.65 mm, which means the recoil proton will travel no more than 0.65 mm, the maximum value of R in Fig. 1.

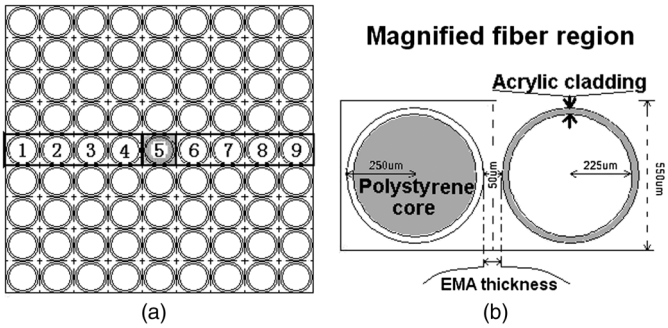

Fig. 3. Structure model of the fiber array detector for Monte Carlo simulation in Geant4 and MCNPX.

Hence, if the diameter of the fiber is of the order of a submillimeter, the recoil proton may penetrate the neighboring fiber and induce the crosstalk effect.

III. Monte Carlo Methods

A. Simulation of Proton Energy Deposition

The simulation of the crosstalk effect in a scintillating fiber array is performed using Monte Carlo code Geant4. MCNPX is also performed to verify the results. In the simulations of the two codes, the scintillating fiber array used is the one previously designed by us. Fig. 3 presents the cross-section of the fiber array. The array is a 9×9 matrix containing 81 BCF-10 fibers based on a single clad model. The fiber has a diameter of 500 μm (450 μm diameter polystyrene core and 25-μm-thick acrylic cladding). The densities of the polystyrene (C_8H_8) core and the acrylic ($C_5H_8O_2$) cladding are 1.05 g/cm^3 and 1.2 g/cm^3, respectively. The dead zone among fibers is filled with optical cement (resin epoxy $C_{11}H_{12}O_3$, 1.1 g/cm^3) acting as EMA [26]. The gap between two adjoining fibers, that is, the EMA thickness, is 50 μm [Fig. 3(b)]. In later simulations, the modeled fiber includes the polystyrene core (94% of the cross-sectional size) and the acrylic cladding (thickness is 3% of the cross-sectional size) [27].

A beam of collimated 14.1 MeV neutrons from outside the array is vertically (into the page) impinged on the whole pixel area where the fiber numbered 5 is located, shown in Fig. 3(a).

Ten million neutrons are used in the simulation. About 65% of them will have interaction with fiber material, and the rest that are transported outside the bounds of the array are killed. In Geant4, the production threshold is defined for electrons, positrons, and gamma rays as a range cut [28]. The code tracks all particles until zero energy. For a recoil proton, when it can no longer produce a δ-ray with energy above the production threshold corresponding to the range cut, it is tracked until zero energy by continuous energy loss. Here, the range cut for the three particles is set as 1 μm, and the corresponding energy thresholds in individual materials of the fiber array are all smaller than 3 keV. In MCNPX, the energy cutoffs of gamma ray, electron, and positron are all set to be 1 keV, and the energy deposition of the proton will be recorded until the proton energy decreases to 1 keV.

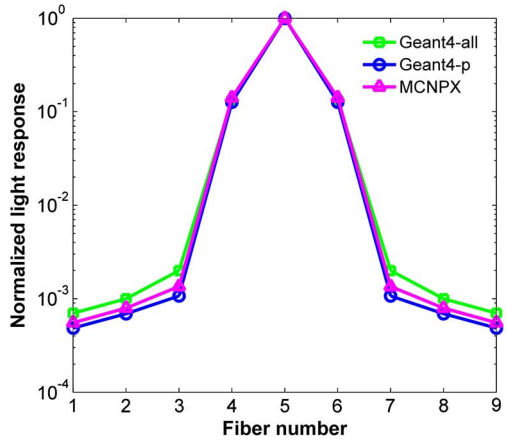

Fig. 4. Maximum normalized light response in the nine fibers calculated by MCNPX and Geant4 with an RSD smaller than 5%.

The energy depositions of the proton in the nine fibers, numbered as 1 to 9, are recorded by the two codes. The results of Geant4 and MCNPX in this case agree well with a relative deviation of less than 3%.

B. Simulation of Light Output

The crosstalk effect exists in the light response signal. Therefore, the light output is simulated by the two codes. In Geant4 code, the details about the scintillation model have been described in Section II. The optical processes available in the code are also used. Besides the scintillation process, transition radiation and Cerenkov process are considered in the production of optical photons. The propagation of the light in fiber is based on the total internal reflection at the interface of fiber core and cladding. According to [27], the refractive indices of the core and the cladding are 1.6 and 1.49, respectively. The attenuation length of scintillation light in the fiber core is set to be 2 m. The absorption and emission spectra, as well as the fast and slow components of the scintillation, of the fiber core are also set. A photon-sensitive detector [17] is installed to tally the photons at the end face of the fiber array. In Fig. 4, the light response obtained only for the light produced by recoil protons is labeled as Geant4-p. In addition, the light response of all the secondary particles involved in the light production is calculated and it is labeled as Geant4-all. We take advantage of symmetry (about the irradiated fiber) of the light response curve to improve the statistics. In later simulations, the same treatment is used for the distributions with expected symmetry. Since MCNPX can obtain only energy deposition of protons, further calculation is carried out to convert the proton energy depositions to photon yield in each fiber. The calculation process is based on the same semi-empirical Birks formula as that used in Geant4. The specific energy loss is given by MCNPX and the required dE/dx of protons with different energies in polystyrene is provided by Stopping and Ranges of Ions in Matter (SRIM) [29]. Then, the light response produced by protons in the nine fibers is obtained using (2). The curve of the maximum normalized light response is labeled as MCNPX in Fig. 4. Good agreement can be seen between the MCNPX and Geant4-p curves.

C. Production and Detection Threshold

As previously mentioned in Section III-A, Geant4 code tracks all particles until zero energy. If the energy of a recoil proton is lower than the production threshold, no secondary δ-rays are generated and the scintillation light is directly produced by the continuous energy loss of the proton. To obtain a reliable simulation result, the production threshold (range cut) should be set as low as possible. In the later simulations, the range cuts for electron, positron, and gamma ray are set to be 1 μm.

In a real detector system, the detection threshold is often used to guard against the noise signal. The production threshold method in Geant4 is not a detector threshold, because it does not kill the particles. To study the influence of detection threshold on the useful neutron signal and proton-induced crosstalk signal, a photon detection threshold is implemented in the simulation. Only the photons above the threshold reaching the end of the fiber will be recorded as the light signal. The simulated light response shows that each incident neutron (not n-p interaction) produces an average of 130 photons, and 17 photons, at the end of the irradiated fiber numbered 5 and 4, respectively. Therefore, a 25-photon detection threshold for single neutron imaging can guard against the recoil proton-induced crosstalk signal (17 photons). Here, the 27-photon detection threshold and 0.1 MeVee threshold are equivalent (8000 photons per MeVee and 3.4% trapping fraction of the cylindrical fiber).

In an ICF experiment, the detection threshold is set to be about one neutron per fiber [1], [30]. However, the actual neutron yield and neutron flux distribution are unknown. The number of time-unresolved neutrons impinging on each fiber may range from dozens to hundreds [6], and the photon detector is working at current mode [30]. Therefore, it is impossible to discriminate the recoil protons-induced crosstalk signal from the useful signal by a reasonable detection threshold. In later simulations, the detection threshold is not used.

D. Fiber Length and Light Output

The recoil protons produced in the central fiber numbered 5 can hardly penetrate into the fibers far away, such as 1, 2, and 3. The number of photons produced in fiber 5 or its adjacent fibers numbered 4 and 6 are two orders of magnitude higher than those of fibers at a further distance. The weak light in those far-away fibers is produced by the scattered neutrons, and it degrades image contrast [12]. This kind of scattered neutron-induced crosstalk is hard to prevent by using EMA. Employing the array with short fibers, for example, 5 cm in length, is a good way to reduce this kind of crosstalk effect [3]. It should be noted that the recoil proton-induced crosstalk is not sensitive to the fiber length. The dependence of light distribution (all secondary particles) of the array on fiber length is calculated by Geant4 and shown in Fig. 5. It can be found that the crosstalk effect, existing in the light response near the irradiated fiber, is unchanged with the fiber length, when the length is several centimeters which is much longer than the maximum trace (1.5 mm by SRIM) of recoil protons in polystyrene. In later simulations, the fiber length is set to be 10 cm.

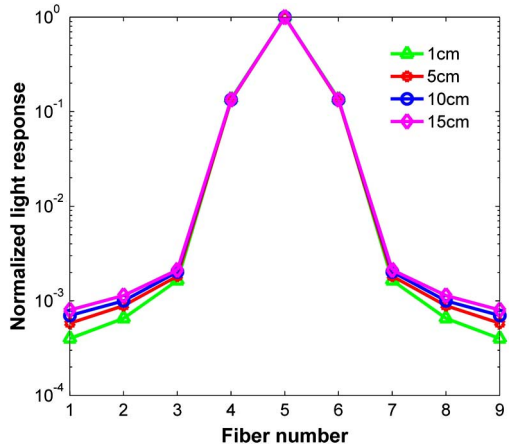

Fig. 5. Dependence of light response (maximum normalized) in the nine fibers on fiber length (1, 5, 10, and 15 cm).

IV. Modulation Transfer Function and Spatial Resolution

The implementation of EMA among fibers improves the spatial resolution by reducing the crosstalk effect. However, installing EMA inevitably extends the pixel (fiber and EMA) dimension and, thus, deteriorates the intrinsic spatial resolution. To measure the performance of the scintillating fiber array detector using EMA, it is necessary to implement a reliable procedure for spatial resolution determination. Generally, the full width at half maximum (FWHM) of the light response distribution is regarded as the spatial resolution. However, as shown in Fig. 2, the expected light response does not exceed 600 μm, which includes no more than three data points. The response shows step changes because the fiber has a diameter of several hundred microns, which is too broad to reflect the response continuously. This may lead to unreliable resolution. In a previous study [7], the resolution is calculated by $\sqrt{(2\delta_{\rm pix})^2+\delta_{\rm rec}^2}$, where $\delta_{\rm pix}$ is the pixel size and $\delta_{\rm rec}$ is the FWHM of average light response induced by the recoil protons. It should be noted that this theoretical resolution can only be achieved in a perfectly coherent capillary array, and this formula is also unsuitable for a heterogeneous fiber array containing plastic and high-Z EMA.

Using the slanted-slit method [31], a synthesized line-spread function (LSF) of the detector can be calculated from the slit image. The obtained LSF can be Fourier transformed to the presampling modulation transfer function (MTF) which describes the resolution power of the detector. The greater the crosstalk effect, the smaller the MTF value will be. The method is illustrated by simulation. A slit neutron source releases 10^6 collimated neutrons which are vertically impinged on an array with 6400 square plastic fibers of 100 μm in side length. The simulation is repeated 30 times, and a slit image is obtained every time. The obtained 30 images are stacked together to produce the image for a total of 3×10^7 neutrons, shown in Fig. 6(a). The relative standard deviation (RSD) of Fig. 6(a) was obtained. The middle row of the RSD is shown in Fig. 6(b). The number of incident neutrons 3×10^7 ensures the RSD to be smaller than 0.1. Then, the 1D-LSF is synthesized and shown in Fig. 6(c). The

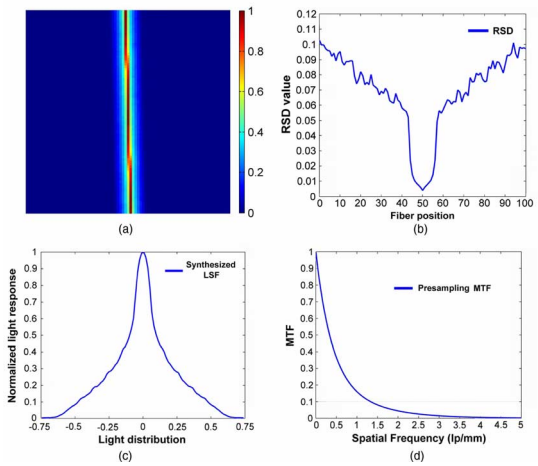

Fig. 6. Graphical illustration of the calculation procedure of the MTF for the array with 6400 square plastic fibers of 100 μm in side length. (a) The slanted slit neutron image (b) RSD of the image. (c) The synthesized LSF. (d) The presampling MTF.

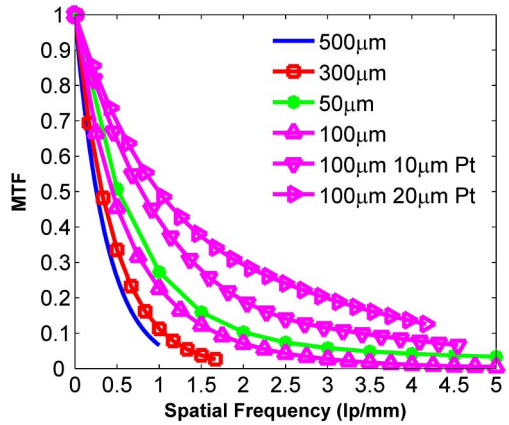

Fig. 7. MTF as a function of the spatial frequency for 500, 300, and 100 μm (without or with 10 and 20 μm Pt-EMA)-size square fiber array.

corresponding presampling MTF with RSD <0.02 is given in Fig. 6(d). Therefore, 3×10^7 is chosen to be the number of neutrons used in later simulations.

Rayleigh's criterion [32] is employed here to define spatial resolution. According to the criterion, two lines can barely be resolved if the two line patterns overlap and the dip value between the same pattern peaks is 81% of the peak value. The corresponding distance between the lines is the resolution. In this condition, MTF is 0.1 at the spatial frequency related to this resolution. According to [33], MTF is defined as

$$\mathrm{MTF} = \frac{M_{\mathrm{captured}}}{M_o} = \frac{\frac{Ic_{\max}-Ic_{\min}}{Ic_{\max}+Ic_{\min}}}{\frac{Io_{\max}-Io_{\min}}{Io_{\max}+Io_{\min}}} \qquad (2)$$

where M_{captured} and M_o are the modulations of the captured image by the array detector and the original image of neutron distribution, respectively. $Ic_{\max}$ and $Ic_{\min}$ are the maximum and minimum intensities of the captured image, while $Io_{\max}$ and $Io_{\min}$ are of the original image.

In the case that two lines can barely be resolved, $Ic_{\max}$ and $Ic_{\min}$ are 1 and 0.81, while $Io_{\max}$ and $Io_{\min}$ are 1 and 0, respectively. The corresponding MTF is calculated to be 0.1 by (2). Therefore, the frequency obtained when MTF decreases to 0.1 is the highest resolvable frequency. It can be read from Fig. 6(d) that the resolution of the detector is about 1.7 lp/mm.

V. EMA and Fiber Arrays

Fig. 7 shows the MTF of the array detectors, each composed of 6400 square plastic fibers. The side length of the fibers in each array is 50, 100, 300, or 500 μm. The MTF of 50 μm fibers is in good agreement with the result in [34]. A common way to improve the resolution is to use thinner fibers. Unfortunately, for the array with thin fibers, the best resolution defined by the Nyquist sampling theorem, which should be two pixel sizes, cannot be achieved due to the crosstalk induced by recoil protons. For example, the spatial resolution of the 100 μm fiber array is not defined by the Nyquist sampling theorem to be 5 lp/mm, but only 1.7 lp/mm (MTF $= 0.1$). Using thinner fibers of 50 μm, the resolution is improved by 23% to 2.1 lp/mm. In contrast, the use of 10 μm Pt-EMA improves the resolution to about 3.4 lp/mm.

In order to show the real resolution of the detector at the experimental condition [6] and the improvement by using EMA, two radiographic images captured by the 100 μm square fiber array with 10 μm Pt-EMA or without are given in Fig. 8(a) and (b). The target source, as shown in Fig. 8(c), includes several line-pairs releasing collimated incident neutrons. In Fig. 8(b), the line pair of 1.7 lp/mm can be resolved. When the Pt-EMA is used, the resolution is evidently improved and the line pair of 3.1 lp/mm can be resolved in Fig. 8(a).

A. EMA Material

For selecting the suitable EMA material, nine kinds of substances are set as candidates. The stopping power for the proton is calculated by SRIM, and the results are shown in Table I. The material with good performance in blocking protons shows a small penetration depth. The penetration depth decreases with the material density and atomic number. Therefore, the high-Z material platinum (Pt) is used as EMA material in later simulations.

The penetration depth of 10 MeV protons in Pt is more than 100 μm. In practice, the direction of incident neutron is parallel to the fiber axis, and the recoil protons are obliquely impinged on the Pt-EMA. Therefore, the actual thickness of Pt-EMA should be less than 100 μm. It should be noted that the EMA is an extra coat of the scintillating fiber. Each fiber has the scintillation core and cladding. The light is guided along the fiber core by total internal reflection at the interface between core and cladding. So the optical properties as well as the light propagation of the fiber will not be affected by the EMA material.

There is a report about the use of high-Z paint as EMA [5]. The performance of this EMA should be highly dependent on the mass percentage of the high-Z material in the paint. A simulation is performed by using the array detector composed of 6400 square plastic fibers with a side of 100 μm and a length of 10 cm for a quantitative study. The MTF is obtained when 10 μm paint of different Pt mass fraction is used, as shown in Fig. 9. It can be observed that the pure (100%) 10 μm Pt has the best performance in improving the resolution from 1.7 to 3.4 lp/mm.

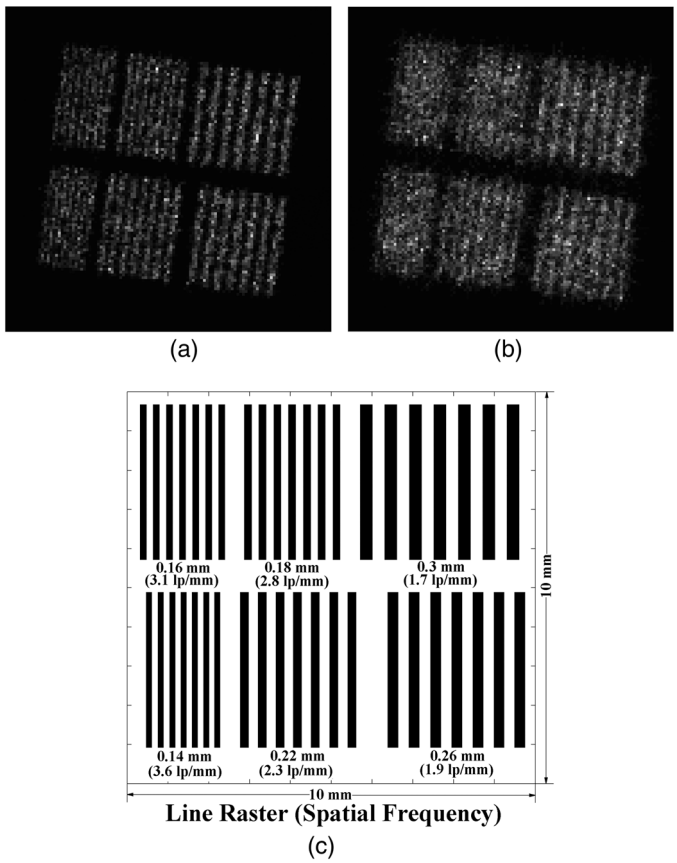

Fig. 8. Simulated neutron radiographs captured by 100 μm square fiber array with 10 μm Pt-EMA or without, 300 neutrons per fiber and one neutron detection threshold for simulating the actual imaging conditions. (a) The radiograph with 10 μm Pt-EMA. (b) The radiograph without EMA, (c) The binary collimated source, including six line pairs (1.7 to 3.6 lp/mm).

TABLE I
PENETRATION DEPTH OF 10 MEV PROTONS IN SEVERAL MATERIALS

Materials	Destiny g/cm^3	Penetration depth (mm)
Al	2.71	0.618
Ti	4.5	0.434
Fe	7.9	0.265
Cu	8.9	0.243
Ag	10.5	0.245
Ta	16.6	0.195
Au	18.9	0.173
W	19.4	0.168
Pt	21.5	0.159

The improvement becomes insignificant with the decrease of Pt mass fraction. Using 10 μm 75% Pt cement, EMA can only improve the resolution to 1.8 lp/mm. When Pt mass fraction is less than 75%, the 10 μm EMA may not improve the resolution as it fails to effectively stop recoil protons. In the later simulations, we use pure 100% Pt as EMA material.

B. Gamma Response

Admittedly, the high-Z material affects the sensitivity of the array detector to gamma rays. In our simulation using an array

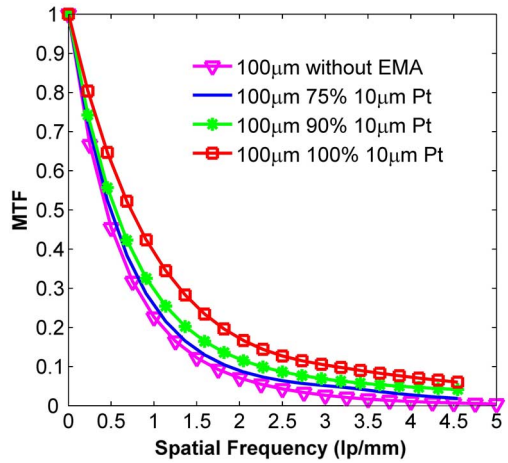

Fig. 9. Dependence of MTF on the Pt mass percentage of EMA of the array with 6400 square plastic fibers with a side of 100 μm and without or with 10 μm EMA of different Pt mass percentages.

with 6400 100 μm square fibers and 20-μm-thick Pt-EMA, the gamma energies are set as 0.1, 1, and 10 MeV. The corresponding LSF and MTF of the array with or without EMA are obtained and shown in Figs. 10 and 11, respectively. In Fig. 10, all of the LSFs are normalized to the peak (position 50) of the distribution labeled as 10 MeV 20 μm Pt. For the irradiated fiber position 50, the light response to 0.1 gamma ray is nearly unchanged when EMA is used, whereas the responses of 1 and 10 MeV gamma rays are increased by about 7% and 5%, respectively. Photoemission and Compton scattering can count for the extra light response to the 1 MeV gamma ray, because extra secondary particles, including scattered gamma rays and electrons, are generated by the two interactions between the incident gamma ray and the Pt-EMA. For the 10 MeV gamma ray, the extra light is also produced by the extra secondary particles, while the main interaction is the pair production. Although Pt-EMA provides extra scattered gamma rays and electrons, it absorbs them as well when they penetrate the EMA and travel into other fibers. For the three gamma ray energies, the light signals produced in the fibers that are far from the irradiated one are suppressed when EMA is used. The use of 20 μm Pt-EMA will result in 30%, 70%, and 40% reductions of total light outputs of the array for 0.1, 1, and 10 MeV gamma ray detections, respectively.

In Fig. 11, the improvement of MTF and resolution can hardly be found when EMA is used in 0.1 and 10 MeV gamma imaging. For the 0.1 MeV incident gamma rays, the scattered gamma rays will have a short trace in the array and produce photons mainly in the irradiated fiber. For the 10 MeV gamma, 20-μm-thick Pt-EMA cannot effectively minimize the gamma-induced crosstalk near the irradiated fiber. One thing to note is that the EMA can suppress the crosstalk signal far from the irradiated fiber in Fig. 10.

C. Neutron Response

The impinging of a neutron on Pt-EMA may give birth to a scattered neutron and gamma rays by (n, 2n) and (n, γn) reactions with cross section 3 and 1.5 barns, respectively. These secondary particles may produce an extra light signal in the

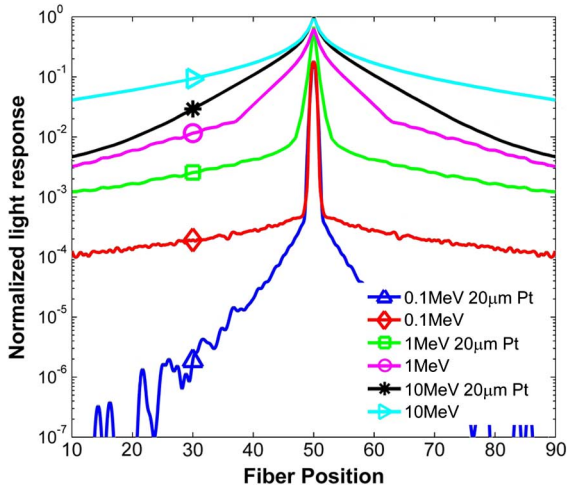

Fig. 10. Dependence of LSF of the 6400 square plastic fibers (100 μm in side length) array on the gamma energy without or with 20 μm Pt-EMA. All of the distributions normalized to the peak of the LSF are labeled 10 MeV 20 μm Pt.

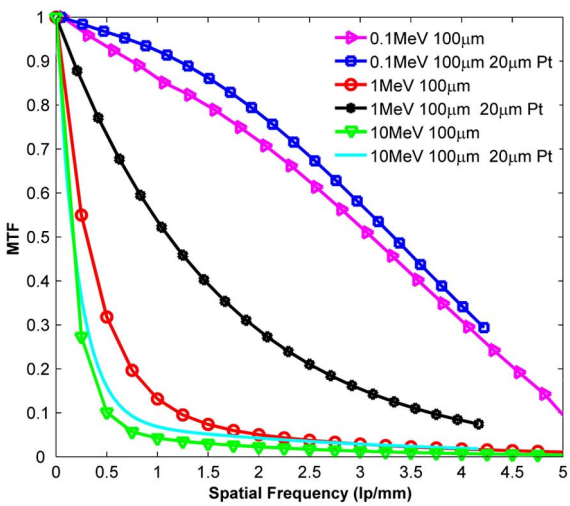

Fig. 11. MTF as a function of spatial frequency of the array with 6400 100 μm square fibers without or with 20 μm Pt-EMA for a gamma of different energies.

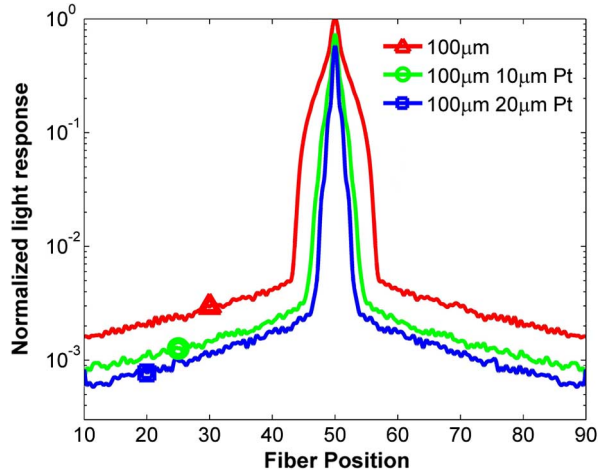

Fig. 12. Dependence of LSF of the array with 6400 100 μm square fibers on the Pt EMA thickness. The distributions were normalized to the max light response without EMA (labeled 100 μm).

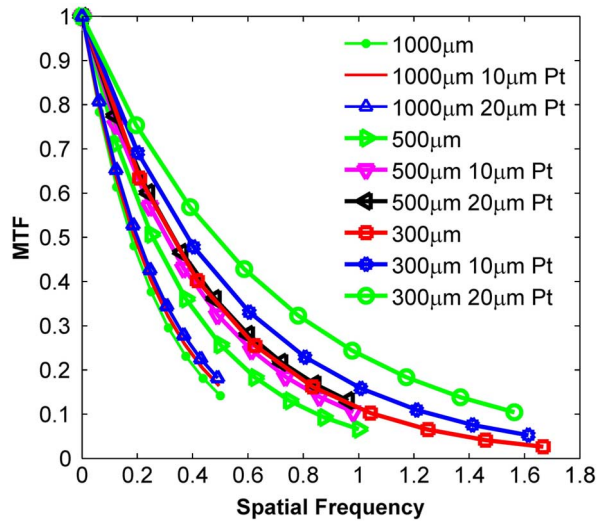

Fig. 13. MTF as function of the spatial frequency for the square fiber array with a fiber of 300, 500, and 1000 μm in the cross-sectional dimension without or with Pt-EMA (10 and 20 μm).

array and deteriorate the image contrast. To study this influence, simulations are performed using arrays comprised of 6400 square 100 μm fibers without Pt-EMA and with 10- or 20-μ m-thick Pt-EMA, respectively. Fig. 12 shows the dependence of LSF on EMA thickness. The improvement of MTF is shown in Fig. 14(b). The presence of Pt-EMA reduces the light response of the irradiated fiber by 25% (10 μm) and 40% (20 μm). It decreases the recoil proton crosstalk near the central irradiated fiber. In the fibers far from the irradiated one, the signal induced by the scattered neutron is also suppressed. This occurs because the recoil protons, produced by the scattered neutrons, are absorbed in EMA.

D. EMA Performance

The resolution is limited by two issues: MTF and the Nyquist sampling theorem. When MTF is smaller than 0.1, the line pair at the corresponding spatial frequency cannot be resolved. In this case, the resolution is related to the frequency when MTF decreases to 0.1. When MTF is larger than 0.1, it will be cut off at the highest frequency defined as $\frac{1}{2(Pixel\_size)}$ by the Nyquist sampling theorem. In this case, EMA may deteriorate the resolution since it increases the pixel area. For example, in Fig. 13, the MTF of the array with 1000 μm fibers is larger than 0.1. The highest spatial frequency, that is, the Nyquist frequency of the array is 0.5 lp/mm. The corresponding resolution is therefore two pixels, namely, 2 mm. The use of EMA will enlarge the pixel size and decrease the resolution. For the arrays of fibers with a cross-sectional size larger than 500 μm, the primary factor limiting the resolution is not the recoil protons but the Nyquist sampling theorem. As a result, it is not recommended to use Pt-EMA in this case.

We can infer from Fig. 13 that EMA is more suitable for the arrays of fibers with smaller cross-sectional dimensions, less than 300 μm here in our simulation. Using EMA, instead of replacing the fibers for thinner ones, improves the resolution.

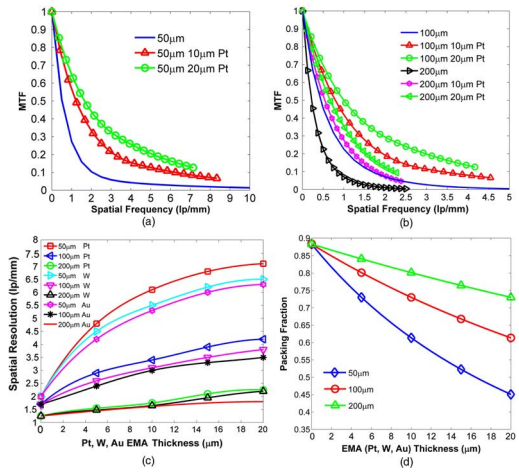

Fig. 14. Simulation results (MTF (Pt), resolution (Pt, W, and Au) and packing fraction) of square scintillating fiber array with a fiber cross-sectional dimension of 50, 100, and 200 μm and without or with EMA. (a) MTF of 50 μm arrays versus spatial frequency. (b) MTF of 100 and 200 μm arrays versus spatial frequency. (c) Resolution versus EMA (Pt, W, and Au) thickness. (d) Packing fraction versus EMA thickness.

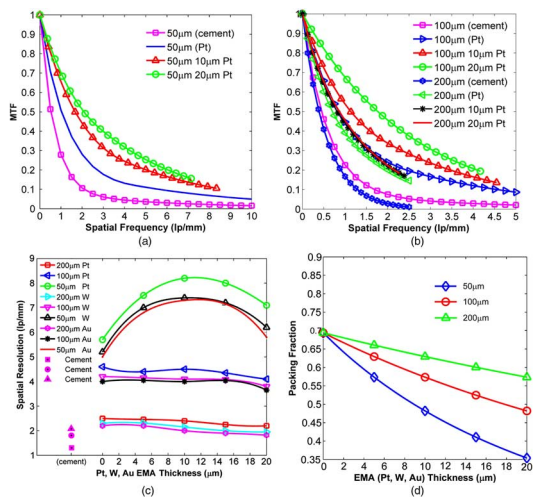

Fig. 15. Simulation results (MTF (Pt), resolution (Pt, W, and Au), and packing fraction) of the square packing cylindrical scintillating fiber array with a fiber diameter of 50, 100, and 200 μm and without or with EMA. (a) MTF of 50 μm arrays versus spatial frequency. (b) MTF of 100 and 200 μm arrays versus spatial frequency. (c) Resolution versus EMA (Pt, W, and Au) thickness. (d) Packing fraction versus EMA thickness.

Nevertheless, it leads to extra dead zone in the arrays and decreases the packing fraction. The packing fraction here is defined as the proportion of the area occupied by the core (94% of the fiber cross-sectional size) of scintillating fibers. To study the overall performance of Pt-EMA, we simulate three prototypes of a scintillating fiber array, which are composed of cylindrical fibers in square and hexagonal packing arrangements and square fibers, respectively. The cross-sectional dimensions of the fibers are set to be 50, 100, and 200 μm. Both spatial resolution and packing fraction are taken into account.

The simulation results for the square fiber arrays are presented in Fig. 14. Fig. 14(a) and (b) gives the MTF of the three arrays with or without EMA. Fig. 14(c) shows the dependence of the resolution on Pt-EMA thickness. As a comparison, the performances in resolution using pure tungsten (W) and gold (Au) EMA are also given in Fig. 14(c). Fig. 14(d) demonstrates the change of packing fraction with respect to EMA thickness. The Pt-EMA shows the best performance and can evidently improve the spatial resolution, especially for the 50 μm fiber array. The resolution using Pt-EMA is roughly 10% higher than that with W-EMA of the same thickness. Compared with Au-EMA, W-EMA is better. For the three EMAs, the growth tendency of resolution is slower when the EMA thickness gets larger. The packing fraction decreases with the EMA thickness, especially in the 50 μm fiber array. For EMA thickness, 10 μm makes a suitable tradeoff between packing fraction and spatial resolution. The use of 10 μm Pt-EMA for the 50, 100, and 200 μm square fiber arrays can increase the resolution by about 300%, 200%, and 50% on the cost of losing 28%, 20%, and 18% packing fraction, respectively.

Fig. 15 illustrates the simulation results for the square packing cylindrical (SPC) fiber arrays. For cylindrical fiber arrays, regardless of how the fibers are packed, there will be an original dead zone among fibers. In Fig. 15(a), the curve marked 50 μm (cement) represents the MTF of the 50 μm array with cement in the dead zone, and the curve marked 50 μm (Pt) represents the MTF when the dead zone is filled with Pt material. (The EMA thickness is zero.) It is similar in 100 and 200 μm arrays, shown in Fig. 15(b). It should be noted that the EMA thickness defined for the cylindrical fiber array is the gap between two adjoining fibers. Therefore, even if the Pt-EMA thickness is zero, the Pt material in the dead zone can also block the recoil protons and improve the resolution. For example, the spatial resolution of the 50 μm fiber array is improved from 2.1 to 5.8 lp/mm by changing the dead-zone material from cement to Pt, when the EMA thickness is zero [Fig. 15(c)]. The dependence of the resolution on W-EMA and Au-EMA thickness is also shown in Fig. 15(c). The Pt-EMA shows the best performance as expected. When extra EMA (Pt, W, or Au) is added, the resolution first increases and then decreases with EMA thickness. Using 10 μm Pt-EMA for the 50 μm fiber array, the resolution increases from 5.8 to 8.2 lp/mm on the cost of losing 22% packing fraction [Fig. 15(d)], and then decreases to 7.1 lp/mm with the addition of an extra 10 μm (20-μm-thick) Pt-EMA. For the arrays of fibers with larger diameters, extra EMA (i.e., EMA thickness that is more than zero) deteriorates the resolution [Fig. 15(c)]. Therefore, it will be a good choice that the material, such as optical cement, in the dead zone is replaced by the high-Z material without introducing an extra dead zone.

Fig. 16 shows the results for the hexagonal packing cylindrical (HPC) fiber arrays. Substituting Pt for cement can also improve the resolution. The difference of the simulation results between HPC and SPC fiber arrays is due to the difference in their packing formations. The HPC fiber array has a higher packing fraction [Fig. 16(d)]. The energy loss of the recoil proton in the surrounding dead zone is lower in the HPC fiber array, although the gap between two contiguous fibers, which is actually the EMA thickness, is the same in the two packing formations. It can be concluded from Fig. 16(c) and 15(c) that the improvement in resolution using Pt-EMA is higher for the HPC fiber array than for the SPC one.

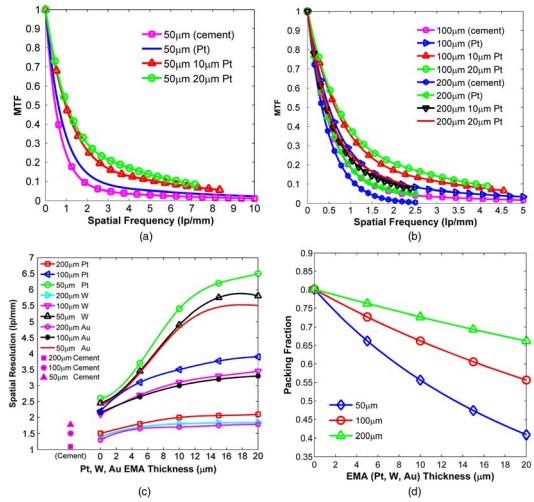

Fig. 16. Simulation results (MTF (Pt), resolution (Pt, W, and Au) and packing fraction) of the hexagonal packing cylindrical scintillating fiber array with a fiber diameter of 50, 100, and 200 μm and without or with EMA. (a) MTF of 50 μm arrays versus spatial frequency. (b) MTF of 100 and 200 μm arrays versus spatial frequency. (c) Resolution versus EMA (Pt, W, and Au) thickness. (d) Packing fraction versus EMA thickness.

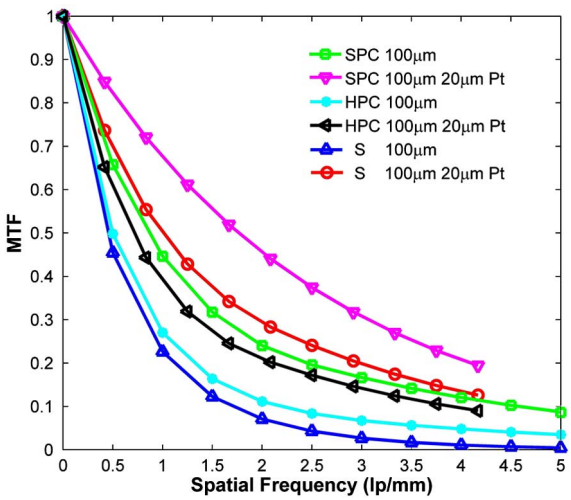

Fig. 17. MTF as a function of the spatial frequency for the array of the square packing cylindrical (SPC) and hexagonal packing cylindrical (HPC) fiber array and the square fiber (S) array (with or without 20 μm Pt-EMA).

The dependence of MTF on the detector prototype is shown in Fig. 17. The HPC fiber array has a higher packing fraction than the SPC fiber array. It has greater crosstalk and lower spatial resolution. The employment of Pt-EMA demonstrates higher resolution improvement in the HPC fiber array than in the SPC fiber array. The square fiber array with the same fiber dimensions displays the highest packing fraction and the worst resolution. Moreover, the improvement of resolution using Pt-EMA for this kind of array is the most evident.

VI. Conclusion and Discussion

The use of Pt-EMA in a scintillating fiber array detector shows a desired crosstalk suppression effect. However, it is not universally applicable. Regarding the fiber arrays simulated in this paper, the improvement of resolution by using Pt-EMA can hardly be found in the arrays with a fiber cross-sectional dimension larger than 300 μm. A decrease in the fiber cross-sectional size leads to an appreciable increase in the crosstalk and a more evident effect of EMA. Hence, EMA is more suitable for the arrays of fibers with cross-sectional dimensions that are smaller than 200 μm. Installing Pt-EMA thicker than 20 μm can suppress the crosstalk effect more effectively. However, the thicker EMA is not always the right solution, because it decreases the packing fraction.

Compared with a hexagonal or square packing cylindrical fiber array, the array of square fibers with the same cross-sectional dimension has the highest packing fraction. Employing 10-μm-thick Pt-EMA for the array with a square fiber size smaller than 200 μm can improve the resolution up to 100%. Furthermore, the square packing cylindrical fiber array presents the lowest crosstalk, and its spatial resolution decreases following the introduction of Pt-EMA. It may be a good choice to replace the material in the dead zone, such as optical cement, by high-Z materials for this kind of array.

The dead zone filled with EMA will lead to a missing area in the grid pattern on the light image [35]. Further studies need to be conducted for the recovery of the missing area.

Pt has the best performance to stop recoil protons, while it may cost tens of thousands of dollars to fabricate pure Pt-EMA for an array. Tungsten is a good lower-cost candidate EMA material of about several hundred dollars. Substituting W-EMA for the Pt-EMA in an array will result in 5%–10% resolution loss. Gold is not considered EMA material because it has no advantages in cost and resolution improvement. The two materials–platinum and tungsten–will be manufactured as EMA in small arrays to compare their performance on resolution improvement, cost, and so on. Magnetron-sputtered deposition and electroplating technology are promising methods to fabricate the EMA film for scintillating fibers. A multiobjective optimal design of the fiber array detector with EMA will be carried out according to the experiments in the near future.

In addition, the method in this research could serve as a reference for the study of EMA performance in multipixel gamma or X-ray detectors.

Acknowledgment

The authors would like to thank R. F. Yuan from Northwest Institute of Nuclear Technology (NINT) of China and Y. L. Wu of the Nuclear and Radiation Safety Centre of the State Environmental Protection Administration of China for their useful discussions and suggestions.

References

[1] T. Caillaud *et al.*, "Development of the large neutron imaging system for inertial confinement fusion experiments," *Rev. Sci. Instrum.*, vol. 83, pp. 033502-1–033502-7, Mar. 2012.

[2] L. Disdier *et al.*, "Inertial confinement fusion neutron images," *Phys. Plasmas*, vol. 13, pp. 056317-1–056317-6, May. 2006.

[3] C. A. Barrera, "Experimental component characterization, Monte Carlo based image generation and source reconstruction for the neutron imaging system of the national ignition facility," Ph.D. dissertation, Dept. Nucl. Eng., Univ. CA., Berkeley, USA, 2007. [Online]. Available: https://e-reports-ext.llnl.gov/pdf/351634.pdf

[4] L. Disdier, R. A. Lerche, J. L. Bourgade, and V. Yu. Glebov, "Capillary detector with deuterated scintillator for inertial confinement fusion neutron images," *Rev. Sci. Instrum.*, vol. 75, pp. 2134–2139, Jun. 2004.

[5] D. Ress, R. A. Lerche, R. J. Ellis, and S. M. Lane, "Design of a neutron penumbral-aperture microscope with 10 μm resolution," *Rev. Sci. Instrum.*, vol. 61, pp. 3184–3186, Oct. 1990.
[6] D. Ress, R. A. Lerche, R. J. Ellis, G. W. Heaton, and D. E. Lehr, "High-sensitivity scintillating fiber imaging detector for high-energy neutrons," *Rev. Sci. Instrum.*, vol. 61, pp. 4943–4948, Oct. 1995.
[7] L. Disdier, A. Rouyer, A. Fedotoff, J. L. Bourgade, F. J. Marshall, V. Yu. Glebov, and C. Stoeckl, "Neutron imaging of ICF target plasmas," *Rev. Sci. Instrum.*, vol. 74, pp. 1832–1836, Mar. 2003.
[8] L. Disdier *et al.*, "High-resolution neutron imaging of laser imploded DT targets," *Nucl. Instrum. Meth. Phy. Res. A*, vol. 489, pp. 496–502, Aug. 2002.
[9] M. D. Wilke *et al.*, "The National ignition facility neutron imaging system," *Rev. Sci. Instrum.*, vol. 79, pp. 10E529-1–10E529-5, Oct. 2008.
[10] D. N. Fittinghoff *et al.*, "Performance improvements to the neutron imaging system at the national ignition facility," Livermore, CA, USA, Rep. LLNL-TR-503351, 2011. [Online]. Available: https://e-reports-ext.llnl.gov/pdf/518889.pdf
[11] T. Nishitani, M. Isobe, G. A. Wurden, R. E. Chrien, H. Harano, K. Tobita, and Y. Kusama, "Triton burn up measurements using scintillating fiber detectors on JT-60U," *Fusion Eng. Des.*, vol. 34, pp. 563–566, Mar. 1997.
[12] I. Mor *et al.*, "Parameters affecting image quality with Time-Resolved Optical Integrative Neutron (TRION) detector," *Nucl. Instrum. Meth. Phy. Res. A*, vol. 640, pp. 192–199, Jun. 2011.
[13] U. Hampel *et al.*, "High resolution gamma ray tomography scanner for flow measurement and non-destructive testing applications," *Rev. Sci. Instrum.*, vol. 78, pp. 103704-1–103704-9, Oct. 2007.
[14] C. S. Levin, M. P. Tornai, S. R. Cherry, L. R. MacDonald, and E. J. Hoffman, "Compton scatter and X-ray crosstalk and the use of very thin intercrystal septa in high-resolution PET detectors," *IEEE Trans. Nucl. Sci.*, vol. 44, no. 2, pp. 218–224, Apr. 1997.
[15] R. Melnyk and F. A. Dibianca, "Monte Carlo study of X-ray cross-talk in a variable resolution X-ray detector," in *Proc. SPIE*, 2003, vol. 5030, pp. 694–701.
[16] S. Tang, Q. Ma, J. Fang, Z. J. Yin, and D. Zhu, "Simulation study of energy absorption of X-rays and γ-rays in plastic scintillating fiber arrays," *IEEE Trans. Nucl. Sci.*, vol. 54, no. 5, pp. 1773–1778, Oct. 2007.
[17] S. Agostinelli *et al.*, "GEANT4-a simulation toolkit," *Nucl. Instrum. Meth. Phy. Res. A*, vol. 506, pp. 250–303, Jul. 2003.
[18] J. Allison *et al.*, "Geant4 developments and applications," *IEEE Trans. Nucl. Sci.*, vol. 53, no. 1, pp. 270–278, Feb. 2006.
[19] L. Waters *et al.*, MCNPX User's Manual Rep. LA-CP-02-408, Sep. 2002, Los Alamos Nat. Lab..
[20] G. F. Knoll, *Radiation Detection and Measurement*, 4th ed. Hoboken, NJ, USA: Wiley, 2010, pp. 569–579.
[21] Database CNDC. 2001. [Online]. Available: http://www-nds.iaea.org/photo-nuclear/other_files/cndc/
[22] H. Burkhardt, V. M. Grichine, P. Gumplinger, V. N. Ivanchenko, R. P. Kokoulin, M. Maire, and L. Urban, "Geant4 standard electromagnetic package for HEP applications," in *Proc. IEEE Nucl. Sci. Symp. Conf. Rec.*, New York, USA, 2004, vol. 1–7, pp. 1907–1910.
[23] J. B. Briks, *The Theory and Practice of Scintillation Counting*, 1st ed. ed. Oxford, U. K.: Pergamon, 1964, pp. 8–10.
[24] L. T. Angela, "HCAL reconstruction status," presented at the Calice Collaboration Meet., Argonne, IL, USA, Mar. 17–19, 2008. [Online]. Available: http://www.desy.de/~lucaci/Talks/Argonne_March08.pdf
[25] M. A. Charles *et al.*, Determining scintillator response to photons and neutrons by Monte Carlo Livermore, CA, USA, UCRL-12150, Sep. 1964.
[26] T. O. White, "Scintillating fibers," *Nucl. Instrum. Meth. Phy. Res. A*, vol. 273, pp. 820–825, Dec. 1988.
[27] Brochure of Saint-Gobain Scintillation Products, Saint Gobain Crystals and Detectors Ltd. Hiram, OH. U SA, 2005. [Online]. Available: http://www.detectors.saint-gobain.com/uploadedFiles/SGdetectors/Documents/Brochures/Scintillating-Optical-Fibers-Brochure.pdf
[28] *"Physics Reference Manual of Geant4.9.3, CERN"* H. P. Wellisch, M. Maire, and L. Urban, Eds., 2008. [Online]. Available: http://cern.ch/geant4/UserDocumentation/Users-Guides/PhysicsReference-Manual/fo/PhysicsReferenceManual.pdf
[29] J. F. Ziegler, J. P. Biersack, and U. Littmark, "SRIM–The stopping and range of ions in matter (2010)," *Nucl. Instrum. Meth. Phy. Res. B*, vol. 268, pp. 1818–1823, Jun. 2010.
[30] T. Caillaud *et al.*, "A new compact, high sensitivity neutron imaging system," *Rev. Sci. Instrum.*, vol. 83, pp. 10E131-1–10E131-3, Oct. 2012.
[31] H. Fujita, D. Y. Tsai, T. Itoh, K. Doi, J. Morishita, K. Ueda, and A. Ohtsuka *et al.*, "A simple method for determining the modulation transfer function in digital radiography," *IEEE Trans. Med. Imag.*, vol. 11, no. 1, pp. 34–39, Mar. 1992.
[32] A. J. den Dekker and A. van den Bos, "Resolution: A survey," *J. Opt. Soc. AM A*, vol. 14, pp. 547–557, Mar. 1997.
[33] G. D. Boreman, *Modulation transfer function in optical and electro optical systems*, 1st ed. ed. Bellingham, WA, USA: SPIE, 2001, pp. 20–25.
[34] D. Vartsky *et al.*, "Time-resolved fast neutron imaging: simulation of detector performance," *Nucl. Instrum. Meth. Phy. Res. A*, vol. 542, pp. 206–212, Apr. 2005.
[35] R. A. Lerche, D. Ress, R. J. Ellis, S. M. Lane, and K. A. Nugent, "Neutron penumbral imaging of laser-fusion targets," *Laser Part. Beams*, vol. 9, pp. 99–118, Mar. 1991.